A Level Set Theory for Neural Implicit Evolution under Explicit Flows

Ishit Mehta   Manmohan Chandraker   Ravi Ramamoorthi

University of California San Diego

Abstract. Coordinate-based neural networks parameterizing implicit surfaces have emerged as efficient representations of geometry. They effectively act as parametric level sets with the zero-level set defining the surface of interest. We present a framework that allows applying deformation operations defined for triangle meshes onto such implicit surfaces. Several of these operations can be viewed as energy-minimization problems that induce an instantaneous flow field on the explicit surface. Our method uses the flow field to deform parametric implicit surfaces by extending the classical theory of level sets. We also derive a consolidated view for existing methods on differentiable surface extraction and rendering, by formalizing connections to the level-set theory. We show that these methods drift from the theory and that our approach exhibits improvements for applications like surface smoothing, mean-curvature flow, inverse rendering and user-defined editing on implicit geometry.
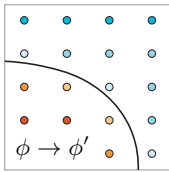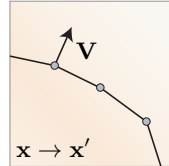
Keywords: Implicit Surfaces, Level Sets, Euler-Lagrangian Deformation

1 Introduction

Recent successes in generative modeling of shapes [13,48,54] and inverse rendering [43,71] are largely driven by implicit representations of geometry parameterized as multi-layer perceptrons (MLPs) (or neural implicits [16]). These networks can compactly represent highly-detailed surfaces at (theoretically) infinite resolution [36,55,61,62]; they are defined continuously in $\mathbb{R}^3$ and are differentiable – enabling their usage in gradient-based optimization [26,71] and learning [2,12,39] methods. Despite these advances, there is still a large body of work in geometry processing, computer vision and graphics which relies on explicit surface representations. Often these mesh-based algorithms are a better choice than their implicit counterparts. For instance, in case of inverse rendering, differentiable renderers for triangle meshes [18,28,29,44,73] are a) faster, b) more accurate, and c) can handle more complex light-transport effects, in comparison to the renderers designed for implicit surfaces [24,43,71]. Similarly, geometry processing algorithms for applications like surface smoothing and deformation [10,56,63] are vastly superior in terms of compute and memory requirements than the ones developed for neural implicit surfaces [69]. Most of these methods, however, are highly specific to mesh geometry and are not easily adaptable to MLP-defined surfaces. Our work is a theoretical attempt to bridge this gap.

We first introduce the following insight: several mesh-based algorithms define an energy-minimization problem that is solved using gradient descent; the gradients used by the optimizer to update the geometry can be viewed as analogous to an instantaneous explicit flow-field ($\mathbf{V}$) applied on the surface. Informed by the literature on fluid simulation [7] and level-sets [46], deformation of a surface with such a flow field depends on the geometry representation.

The *Lagrangian* representation involves tracking the surface explicitly as a set of a points ($\mathbf{x}$) and connections (like triangles). The point-set is discrete and the connectivity is *static*, which keeps the optimization relatively simple; we can separately integrate the field at each point (update vertices $\mathbf{x} \to \mathbf{x}'$). But optimization of the resolution of the surface is non-trivial and can also get unwieldy for problems which involve surfaces with unknown topology.

Alternatively, *Eulerian* descriptions can be used. Each point in space has an object-property ϕ associated with it, like the distance from the surface or its occupancy inside the enclosed volume. The surface here is implicitly defined with *dynamic* connectivity; one can smoothly vary the topology during optimization. Canonically, ϕ is defined only on a discrete voxel-grid and needs to be interpolated for points off the grid. Here, making instantaneous updates to the surface is more involved as it requires changing ϕ values for a large set of points. A neural implicit is a continuous variant of an Eulerian representation. Applying a flow field to such functions is non-trivial as updates are required in the parameter ($\boldsymbol{\theta}$) space as opposed to directly updating ϕ to ϕ'.

We propose a parametric level-set evolution method (§ 4) which propagates neural implicit surfaces according to an explicitly generated flow field. Our method comprises of three repeating steps, 1) A non-differentiable surface extraction method like Marching Cubes [33] or Sphere Tracing [22] is used to obtain a Lagrangian representation corresponding to a neural implicit, 2) A mesh-based algorithm is used to derive a flow field on the explicit surface (§ 4.1), and 3) A corresponding Eulerian flow field is used to evolve the implicit geometry (§ 4.2).

Previous methods [43,51,53] approach the problem of using mesh-based energy functions on Eulerian surfaces with the idea of differentiable extraction of Lagrangian representations. We show these methods are not in accordance with the level-set theory [47] (§ 5). The discussion also yields a more general proof (§ 5.1) for differentiable surface extraction from level set

Fig. 1: Inverse-rendering recovery.

functions with arbitrary gradient norms ($|\nabla\phi| \neq 1$). Our method is more formally connected to the theory and we validate it with experimental observations made on three diverse problem settings, 1) Curvature-based deformation (§ 6.1), where we demonstrate more accurate surface smoothing and mean-curvature flow than previous methods [51,69], 2) Inverse rendering of geometry (§ 6.2), where we show accurate recovery from multi-view images for high-genus shapes without object
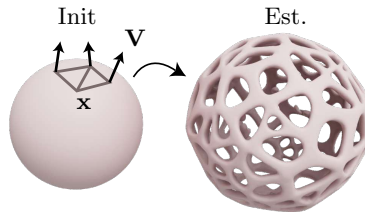
masks as in [43,71] (example in Fig. 1), and 3) User-defined shape editing (§ 6.3), where the implicit surface is deformed $60\times$ faster than previous work [69].

2   Related Work

Coordinate-based MLPs have become a popular choice as function approximators for signals like images, videos and shapes [13,48,55,58,62]. Our work focuses on using MLPs for approximating implicit geometry. Such representations are compact, continuous and differentiable. These advantages are well suited with gradient-descent based optimization and learning problems. Recent developments in generative modeling of shapes [11,37,48,54], 3D consistent image synthesis [12,68], 3D reconstruction [5,59,74] and inverse rendering [26,45,70,71], all rely on representing geometry using MLPs. For a more detailed discussion on recent work regarding coordinate-based representations refer to the survey by Xie *et al.* [67], and for inverse rendering the survey by Tewari *et al.* [65].

There is also a rich literature on geometry processing [8,10,9,57,56] and inverse rendering [4,18,34,42] for explicit surface representations. Yang *et al.* [69] introduce some of the geometry processing ideas to neural implicit surfaces, but the method could be inaccurate (§ 6.1) and slow (§ 6.3).

For inverse rendering applications, differentiable renderers for triangle meshes are used for gradient-based optimization. Physics-based renderers differentiate through a light-simulation process [6,29,44,73] and provide accurate gradients. Alternatively, differentiable rasterization [28,32,50] can be used for high-performance gradient computation, but only for single-bounce rendering models. However, optimizing triangle meshes with gradient-descent is non-trivial. Careful design of the optimization method [18,42] and error functions [34] is required for robust optimization. To circumvent some of these issues, IDR [71] and DVR [43] use implicit surface representations like SDFs and occupancy functions [38] parameterized with MLPs. These methods mitigate some of the topological restrictions, but are not physics-based and are not in accordance with the level-set theory (§ 5.2). We propose an inverse rendering method which uses explicit differentiable renderers for parametrically defined implicit surfaces. The proposed method is not as sensitive to initialization as explicit methods [18,42] are, does not require an object mask like implicit methods [43,71] do, and maintains the ability to vary topology during optimization.

Our method uses the level-set theory [47] as the foundation for optimizing and deforming parametric implicit surfaces. Previous methods [3,41,66] for the applications discussed in this work apply to non-parametric level sets. Perhaps the most related works to our method are MeshSDF [51] and RtS [15]. Compared to MeshSDF, our approach is more formally connected to the theory of level-sets (§ 4), applies to all parametric functions (§ 5.1), and works for a more diverse set of optimization problems like shape editing (§ 6.1, 6.3) and inverse rendering (§ 6.2) – deviating from experimental observations made by Remelli *et al.* [51] on learning-based settings. Compared to RtS [15], we show geometry processing applications along with theoretical parallels (§ 5) between parametric level-set

methods like MeshSDF [51], DVR [43], IDR [71] and the classical theory [46]. Our inverse rendering method is shown to work (§ 6.2) for a set of high-genus shapes with a genus-0 initialization, in contrast to object-pose optimization or small genus changes shown in [15]. Recent work by Munkberg *et al.* [40] and Hasselgren *et al.* [23] also show promise in using explicit differentiable renderers with implicit geometry for inverse problems.

3   Background

Consider a closed surface of arbitrary topology $\partial\Omega$ evolving with respect to time t. We define a Lagrangian representation of this surface with a finite set of k points in $\mathbb{R}^3$ as $\partial\Omega_L = \{\mathbf{x}_i \mid \mathbf{x}_i \sim \partial\Omega; \ \forall i \in \{1, 2, 3, \ldots, k\}\}$. This point-set can be viewed as a triangle mesh if an additional set of connections between the points is provided, and as a point cloud otherwise. Implicitly this surface can also be represented with a family of level-sets $\phi : \mathbb{R}^3 \to \mathbb{R}$, the zero iso-contour of which represents the surface $\partial\Omega_E = \{\mathbf{x} \mid \phi(\mathbf{x}) = 0\}$. ϕ can be arbitrarily chosen, but a canonical choice is a signed-distance function (SDF) which satisfies:

$$\phi(\mathbf{x}) = (\pm) \min_{\mathbf{x}_C \in \partial\Omega} \{||\mathbf{x} - \mathbf{x}_C||_2\}, \tag{1}$$

where $\mathbf{x}_C$ is the closest point on the surface to $\mathbf{x}$ and the sign of $\phi(\mathbf{x})$ denotes whether $\mathbf{x}$ is enclosed $(-)$ within the shape or not $(+)$.

Parameterizing ϕ Analytically defining ϕ for simple and regular shapes is relatively straightforward [49], but is infeasible for most objects. Recent work on 3D reconstruction [43,71] and generative shape modeling [13,48] suggests parameterizing ϕ using a multi-layer perceptron (MLP) with θ as its parameters. The networks are optimized by minimizing an energy function comprised of a distance term [48] and a gradient term [19] enforcing $|\nabla\phi|$ to be 1. We use SIREN [55] as the parametric function of choice, although our method is agnostic to the network parameterization. The network acts approximately as an SDF at the rest state $(t = 0)$, but may not retain the SDF property (Eq. 1) as the surface evolves. We denote this surface as $\partial\Omega_E(\theta) = \{\mathbf{x} \mid \Phi(\mathbf{x}; \theta) = 0\}$, where Φ is parameterized with θ as the weights and biases of the network. For clarity, we use Φ for parametric level-sets and ϕ for non-parametric.

4   Method

We begin the discussion by first characterizing the deformation of surfaces into Lagrangian (§ 4.1) and Eulerian (§ 4.2) settings. We show that gradient descent on energy functions defined for triangle meshes can be viewed as surface deformation under the dynamics of a flow field $\mathbf{V}$, which is *discretely* defined only on the surface points $\partial\Omega_L$. We can use this flow field to deform a *continuous* surface representation using the level-set equation. We extend the level-set equation to the case of parametric level-sets Φ which enables us to use loss functions defined on triangle meshes to deform MLP-defined level-sets.
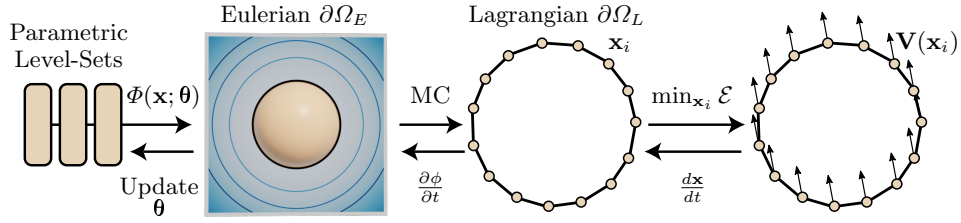
Fig. 2: **Method Overview.** We present a level-set method to evolve neural representations of implicit surfaces. Using Marching Cubes (MC) [33], a Lagrangian surface $\partial\Omega_L$ is extracted from an Eulerian representation $\partial\Omega_E$ encoded in the network parameters $\boldsymbol{\theta}$. An energy function $\mathcal{E}$ is defined on $\partial\Omega_L$ which is minimized using gradient-descent. The gradients of the optimizer together act as a flow-field $\mathbf{V}$ on the surface points $\mathbf{x}$, which is used to evolve the non-parametric ϕ using the level-set equation. The values of ϕ on the surface act as references to update the parameters $\boldsymbol{\theta}$ of the network.

4.1   Lagrangian Deformation

As mentioned earlier, in the Lagrangian setting, the surface is defined with a finite set of points $\partial\Omega_L$. A variety of methods in geometry processing and computer vision define an energy function $\mathcal{E}$ that is minimized to make instantaneous updates to $\partial\Omega_L$. Some recent examples include optimizing point-clouds for view-synthesis [1,52] and triangle-meshes for inverse-rendering of geometry [18,42]. The surface is updated using spatial gradients $\frac{\partial\mathcal{E}}{\partial\mathbf{x}}$, which is well studied in numerical analysis [60] and optimization methods [14]. Through the lens of physics, these gradients induce an instantaneous flow field $\mathbf{V}(\mathbf{x})$, which can be used to evolve the surface by integrating the following ordinary differential equation (ODE):

$$\frac{d\mathbf{x}}{dt} = -\frac{\partial\mathcal{E}}{\partial\mathbf{x}} \to \mathbf{V}(\mathbf{x}). \qquad \lhd \text{ Lagrangian Deformation} \qquad (2)$$

Numerically, this can be done using forward-Euler steps $\mathbf{x}^{t+1} = \mathbf{x}^t + \Delta t\mathbf{V}^t(\mathbf{x})$. This is easy to accomplish if the connectivity of the points remains static. More sophisticated integration schemes can also be used [60]. Here, in case of optimization problems solved using gradient descent, Δt is equivalent to the learning rate. Several works in shape deformation [21] and inverse rendering [42] can be subsumed by this ODE with different definitions for flow $\mathbf{V}$ and time-step Δt. We next show that these readily available energy functions and optimization algorithms defined for explicit surfaces can also be used to optimize MLP-defined level-sets.

4.2   Eulerian Deformation

To avoid the topological complications associated with Lagrangian deformations, we can instead define a corresponding Eulerian deformation field. By definition,

we know for points $\mathbf{x} \in \partial\Omega$, $\phi(\mathbf{x}) = 0$. Using implicit differentiation:

$$\frac{d\phi(\mathbf{x})}{dt} = \frac{\partial\phi}{\partial t} + \frac{\partial\phi}{\partial \mathbf{x}}\frac{\partial \mathbf{x}}{\partial t} = \frac{\partial\phi}{\partial t} + \nabla\phi \cdot \mathbf{V} = 0 \qquad \triangleleft \text{ From 2}$$

$$\Longleftrightarrow \frac{\partial\phi}{\partial t} = -\nabla\phi \cdot \mathbf{V}. \qquad \triangleleft \text{ Eulerian Deformation} \tag{3}$$

This partial differential equation (PDE) is sometimes referred to as the level-set equation [47], the material derivative [7] or the G-equation [35]. We extend this PDE to obtain an evolution method for parametric level-sets Φ. First, for each time step t, we extract a Lagrangian surface representation $\partial\Omega_L^t$ from Φ using MC [33]. Depending on the task at hand, an energy function $\mathcal{E}$ (e.g., photometric error for inverse rendering) is defined on $\partial\Omega_L^t$. Assuming $\mathcal{E}$ is differentiable, we compute $\frac{\partial\mathcal{E}}{\partial\mathbf{x}} = -\mathbf{V}^t(\mathbf{x})$ for each vertex $\mathbf{x}_i \in \partial\Omega_L$. With the flow field $\mathbf{V}^t$, we update the level-set function as we would in the non-parametric case using forward-Euler steps:

$$\phi^{t+1} = \Phi^t - \Delta t \nabla\Phi^t \cdot \mathbf{V}^t. \qquad \triangleleft \text{ From (3)} \tag{4}$$

The time step Δt here is a parameter which is dependent on the dynamics of the flow-field. If $\mathbf{V}$ is highly non-linear, taking smaller steps (i.e., Δt is small) is required, while for a simple field, larger values of Δt should suffice. For each time step, we take the values of non-parametric ϕ^{t+1} as the reference and update the parameters of Φ accordingly. This is achieved by minimizing the following objective:

$$\min_{\boldsymbol{\theta}} J(\boldsymbol{\theta}) = \frac{1}{|\partial\Omega_L|} \sum_{\mathbf{x}\in\partial\Omega_L} ||\phi^{t+1}(\mathbf{x}) - \Phi(\mathbf{x};\boldsymbol{\theta})||^2 , \tag{5}$$

using gradient descent. Since the surface updates are small for each time step, the number of descent steps required is in the order of 10^2. This makes the method convenient for obtaining neural representations of deformed variants of the initial geometry. After each optimization routine, we again extract the Lagrangian surface using MC [33], which is subsequently fed into a mesh-based energy-minimization problem. An overview of our method is shown in Figure 2. For each of the applications we show in § 6, we define $\mathbf{V}^t$ using a corresponding energy function, and minimize J for each time step.

5   Theoretical Comparisons

The level-set method discussed in § 4.2 subsumes two related works, 1) Differentiable iso-surface extraction (MeshSDF) [51], and 2) Differentiable rendering of implicit surfaces (DVR/IDR) [43,71]. We first show that MeshSDF minimizes the level-set objective J defined in (5) with a single gradient-descent step. But the surface does not propagate in agreement with the level-set equation, as outlined in § 5.1. We then show that these two seemingly disparate works (MeshSDF and DVR) are closely related in § 5.2. We end the discussion with an explanation for how DVR deviates from the level-set equation.

5.1 Differentiable Iso-Surface Extraction

Result 1 *Differentiable Iso-Surface Extraction [51] takes a single gradient-descent step to minimize the level-set objective function J (Equation 5).*

Proof. MeshSDF [51] defines a loss-function $\mathcal{L}$ on a triangle mesh extracted using Marching Cubes [33] from an SDF parameterized with an MLP. They use an MLP $\Phi(\mathbf{x}; \boldsymbol{\theta}, \mathbf{z})$ conditioned on a latent-code $\mathbf{z}$ characterizing the shape. Using $\mathcal{L}$ they update the latent-code $\mathbf{z}$, which is different from our goal of updating $\boldsymbol{\theta}$ for an unconditional Φ. To clarify this distinction, we use MeshSDF$^{\boldsymbol{\theta}}$ to denote our variant which updates $\boldsymbol{\theta}$. To update the parameters of the MLP, we compute the following gradient using the chain-rule:

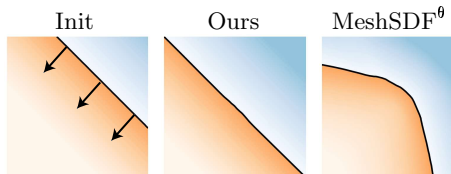Fig. 3: **MeshSDF$^{\boldsymbol{\theta}}$ does not follow the level-set equation**. (*Left*) A planar surface defined implicitly with an MLP is influenced by a flow field in the direction of its normal. The motion attained using differentiable iso-surface extraction (*Right*) is inconsistent with the field. Our method (*Center*) propagates the front as expected.

$$\frac{\partial \mathcal{L}}{\partial \boldsymbol{\theta}} = \sum_{\mathbf{x} \in \partial \Omega_L} \frac{\partial \mathcal{L}}{\partial \mathbf{x}} \frac{\partial \mathbf{x}}{\partial \Phi} \frac{\partial \Phi}{\partial \boldsymbol{\theta}}, \tag{6}$$

where $\mathbf{x}$ are the vertices on the mesh and Φ is an SDF. The first and the third gradient terms on the right are computed using automatic differentiation. The second term $\frac{\partial \mathbf{x}}{\partial \Phi}$ can be approximated as the inverted surface normal $-\mathbf{n}(\mathbf{x}) = -\nabla_{\mathbf{x}} \Phi$ [51], when Φ is an SDF. In the spirit of Lagrangian deformation (Equation 2), $-\frac{\partial \mathcal{L}}{\partial \mathbf{x}}$ acts as an instantaneous flow field $\mathbf{V}$ on the vertices $\mathbf{x}$. The parameters of the MLP are then updated as:

$$\boldsymbol{\theta} \leftarrow \boldsymbol{\theta} - \lambda \frac{\partial \mathcal{L}}{\partial \boldsymbol{\theta}} = \boldsymbol{\theta} - \lambda \sum_{\mathbf{x} \in \partial \Omega_L} \mathbf{V} \cdot \nabla \Phi \frac{\partial \Phi}{\partial \boldsymbol{\theta}}, \tag{7}$$

where λ is the learning rate. Alternatively, we can also update $\boldsymbol{\theta}$ using the objective function defined in Equation 5 using gradient descent:

$$\boldsymbol{\theta} \leftarrow \boldsymbol{\theta} - \lambda \frac{\partial J}{\partial \boldsymbol{\theta}} = \boldsymbol{\theta} - \lambda \sum_{\mathbf{x} \in \partial \Omega_L} 2(\phi^{t+1}(\mathbf{x}) - \Phi(\mathbf{x}; \boldsymbol{\theta})) \left(-\frac{\partial \Phi}{\partial \boldsymbol{\theta}} \right)$$

$$= \boldsymbol{\theta} - \epsilon \sum_{\mathbf{x} \in \partial \Omega_L} \mathbf{V} \cdot \nabla \Phi \frac{\partial \Phi}{\partial \boldsymbol{\theta}}, \quad \triangleleft \text{ From (4)} \tag{8}$$

where ϵ is a constant. The last equivalency is valid when $\phi^{t+1}(\mathbf{x}) - \Phi(\mathbf{x}; \boldsymbol{\theta}) = -\Delta t \mathbf{V} \cdot \nabla \Phi$ (Eq. 4), which is true only for the first gradient descent step. Subsequently, the value of $\Phi(\mathbf{x}; \boldsymbol{\theta})$ changes as the parameters get updated. Comparing (7) and (8), we conclude that the optimization in MeshSDF$^{\boldsymbol{\theta}}$ has the effect of

taking a single gradient-descent step to minimize J. Note that while the proof by Remelli *et al.* [51] assumes Φ is an SDF, the second update equation (8) does not. It is valid for all level-set functions, with no restrictions on the values of the gradient-norm ($|\nabla\Phi|$) and is also valid for occupancy functions [38]. $\square$

However, by taking a single step to update θ, the surface does not propagate in agreement with the level-set equation (3). This is problematic for applications which require the surface to move as intended by the flow-field. An example application is shown in § 6.1. We also illustrate this with a toy example in Figure 3 where a planar surface propagates in the direction of its normal. A more formal discussion is in Result 2.

Result 2 *Dfferentiable iso-surface extraction [51] does not propagate the surface-front as dictated by the flow field.*

Proof. We show this with an example flow field. Consider the surface-front propagating with a constant speed β in the direction of the normal. The corresponding Eulerian deformation is constant across the surface:

$$\frac{\partial \phi}{\partial t} = -|\nabla \phi|\beta = -\beta. \qquad \triangleleft \ \text{Assuming } \phi \text{ is an SDF} \tag{9}$$

With the same flow field, we can estimate the instantaneous change in Φ (parametric) for MeshSDF$^{\theta}$ as:

$$\frac{\partial \Phi}{\partial t} = \frac{\partial \Phi}{\partial \theta}\frac{\partial \theta}{\partial t} = \frac{\partial \Phi}{\partial \theta} \sum_{\mathbf{x}\in\partial\Omega_L} -\beta\frac{\partial \Phi}{\partial \theta} = \frac{\partial \Phi}{\partial \theta}B. \quad \triangleleft \ \text{From (7) and (9)} \tag{10}$$

The term B on the right is constant for every point $\mathbf{x}$ on the surface. The gradient $\frac{\partial \Phi}{\partial \theta}$ is dependent on the position where it is evaluated and hence front-propagation $\frac{\partial \Phi}{\partial t}$ is not constant. On the contrary, we minimize the objective function defined in (5) which ensures that the surface propagation is constant as in (9). $\square$

For the implications of Result 1 and 2, and experimental comparisons, we defer the discussion to § 6.1.

5.2   Differentiable Surface Rendering

An alternate way of extracting a Lagrangian surface $\partial\Omega_L$ from Φ is by computing ray-surface intersections using ray-marching or sphere-tracing [22]. If ray-marching is differentiable [25,31], one can backpropagate gradients from error functions defined on $\partial\Omega_L$ to the parameters θ defining the implicit surface. Recent developments in inverse rendering [38,71] rely on this idea. The explicit surface extracted using ray-marching differs from the one obtained using marching-cubes in two ways, 1) Ray-marching does not extract the connectivity (*e.g.*, triangle faces) among the intersection points. This restricts the usage of loss functions which rely on attributes like the edge-length or differential operators like the Laplacian. 2) The intersection points depend on the camera attributes.

The resolution of the image plane affects the density of points and the viewing direction determines the visibility. As a result, $\partial\Omega_L$ obtained using ray-marching could be sparser than the one obtained marching cubes. Furthermore, as we show in Result 3, by using differentiable ray-marching the parameters get updated exactly as when differentiable iso-surface extraction is used—although with a less favorable Lagrangian representation (sparser and no connectivity). This is in addition to the computational disadvantage associated with ray-marching. We also formally show in Result 4 that surface evolution with differentiable ray-marching is in disagreement with level-set theory for tangential flows.

Result 3 *Surface evolution using differentiable ray-marching of parametric implicit surfaces [38,71] is the same as using differentiable iso-surface extraction [51] when the viewing direction $\mathbf{v}_u$ is parallel to the normal $\mathbf{n}$ at the intersection point $\mathbf{x}_u$. The parameters θ for the level-set function Φ are updated as:*

$$\theta \leftarrow \theta - \lambda \sum_{\mathbf{x}_u} \mathbf{V} \cdot \nabla\Phi \frac{\partial\Phi}{\partial\theta}, \tag{11}$$

where $\mathbf{x}_u$ are the visible points and $\mathbf{V}$ is the flow field. Comparing (11) and (7), the gradient-descent step is the same. As in the case of MeshSDF$^\theta$, here the surface is evolved with a single step in the parameter space. We provide a more detailed proof for (11) in the Appendix.

Result 4 *Differentiable ray-marching of parametric implicit surfaces [38,71] disagrees with the level-set equation for tangential components $\mathbf{V}^\perp$ of the flow field $\mathbf{V}$. The change in parameters $\Delta\theta$ is:*

$$\Delta\theta = \lambda \sum_{\mathbf{x}_u} \pm|\mathbf{V}^\perp| \tan(\arccos(\nabla\Phi \cdot \mathbf{v}_u)) \frac{\partial\Phi}{\partial\theta} \neq 0, \tag{12}$$

which could be non-zero. A detailed proof is in the Appendix. Referring to Eq. 3, for tangential flows the surface should not undergo any deformation, i.e. $\frac{\partial\phi}{\partial t} = 0$. However, since θ gets updated as in (12), the surface *does* deform. We instead minimize the objective function J (Eq. 5) which is 0 for a tangential field. We show an example
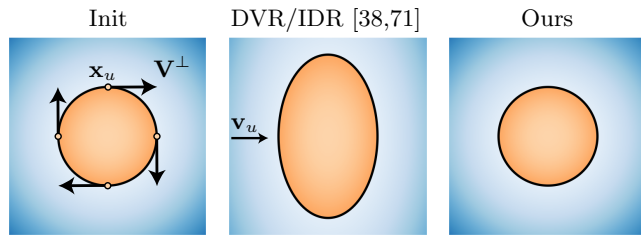

Fig. 4: **Tangential flow fields may deform surfaces when DVR/IDR is used for surface extraction.** (*Left*) A parametric Eulerian circle undergoes tangential deformation $\mathbf{V}^\perp$ at surface points $\mathbf{x}_u$. (*Middle*) Using differentiable surface rendering, the surface deforms incorrectly. (*Right*) Our method agrees with the level-set equation and the resultant deformation is the identity.

of tangential deformation in Figure 4. Experimental comparisons in § 6.2 validate that deforming Φ accurately is critical for applications like inverse rendering.

6   Applications

We focus on validating the proposed theory with computer graphics models in three different settings, 1) Curvature-based deformations (§ 6.1), which can be used to smooth/sharpen features and apply curvature defined flows on implicit surfaces, 2) Inverse rendering of geometry (§ 6.2), where a differentiable renderer for explicit geometry can be used to evolve implicit surfaces, and 3) User-defined deformations (§ 6.3), where a user can specify alterations for a given object.

6.1   Curvature-based Deformation

To apply surface smoothing on parametric implicit surfaces, we first define a corresponding explicit force field. For the extracted Lagrangian surface $\partial \Omega_L$ at each time step, we minimize the Dirichlet-energy functional on the surface. In the continuous setting, this is defined as:

$$\mathcal{E}(\partial \Omega) = \int_{\partial \Omega} ||\nabla \mathbf{x}||^2 \, d\mathbf{x}. \qquad (13)$$

Minimizing $\mathcal{E}$ can be shown [8] to induce the following explicit flow-field on the surface:

$$\frac{\partial \mathbf{x}}{\partial t} = \mathbf{V}(\mathbf{x}) = \lambda \Delta \mathbf{x} = -2\lambda \kappa(\mathbf{x})\mathbf{n}(\mathbf{x}), \qquad (14)$$

where λ is a scalar diffusion coefficient, Δ is the Laplace-Beltrami operator and $\mathbf{n}$ is the normal. κ is the mean-curvature, which for an implicit surface is defined as the divergence of the normalized gradient of ϕ (*i.e.*, $\nabla \cdot \frac{\nabla \phi}{|\nabla \phi|}$) [46]. It is equivalent

Fig. 5: **The laplacian $\Delta \Phi$ of an MLP-defined level-set function is noisy**. We show the mean-curvature values for a parametric level-set function of a square. Large values are observed for a zero-curvature surface.

to computing the laplacian $\Delta \Phi$ of the MLP using automatic differentiation. In Figure 5 we show that such an estimation of the laplacian is noisy—significant magnitudes are observed even for surfaces with zero curvature.[1] Instead of using (14) as it is, which requires estimating $\Delta \Phi$, we approximate $\mathbf{V} = \lambda \Delta \mathbf{x} \approx \lambda \mathbf{L}\mathbf{x}$; where $\mathbf{L}$ is the discrete Laplacian we can compute using the Lagrangian surface. Note that this is feasible only because of the hybrid (Eulerian+Lagrangian) nature of our method. We use the flow-field to update Φ using the method outlined in § 4.2. Figure 6 shows qualitative comparisons for smoothing applied on two surfaces. We show a comparison with a method which applies deformation using the continuous Laplacian ($\Delta \Phi$) (NFGP) [69]. When $\mathcal{E}$ is minimized using MeshSDF$^\theta$ [51], the deformation is not curvature based and high-frequency features are retained during the evolution.

Equation (14) is referred to as mean-curvature flow [17]. Since our method deforms the surface in accordance with the flow-field, we can use (14) to apply
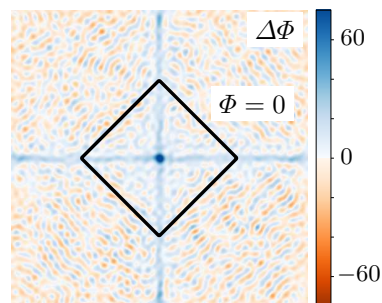
---

[1] This might be due to the unconstrained Lipschitz constants of MLPs [30].

Init   MeshSDF$^\theta$ [51]   NFGP [69]   Ours
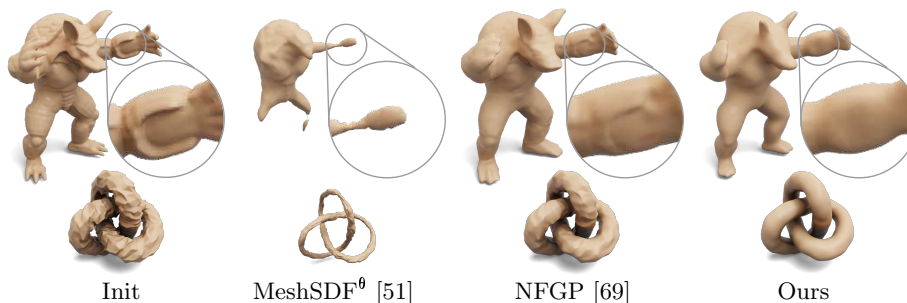
Fig. 6: **Surface smoothing on parametric level-sets.** We apply surface smoothing on an MLP-defined implicit surface by minimizing Dirichlet energy on the corresponding explicit surface. We use a discrete Laplacian to define a flow-field on the surface; NFGP [69] uses its continuous counterpart and preserves too many high-frequency details. MeshSDF$^\theta$ [51] fails to smoothen the surface.

mean-curvature flow on a parametrically defined ϕ. Yang *et al.* [69] minimize an objective function which is handcrafted for a specific level-of-smoothness. Applying curvature-based flow is infeasible with their method since it would require a new optimization objective for each level-of-smoothness. As MeshSDF$^\theta$ [51] does not evolve the surface according to the level-set equation, the flow obtained with it is incorrect. We show an example flow on a genus-0 surface in Figure 7.

6.2   Inverse Rendering of Geometry

We propose an inverse-rendering method which uses a differentiable renderer designed for triangle meshes to optimize geometry defined using parametric level-sets. As in the case of recent methods [4,43,71], we use an analysis-by-synthesis approach. A photometric error comparing the captured and the rendered images is minimized using gradient descent. The gradients of the error function are used to define an explicit flow-field. A corresponding Eulerian deformation field is
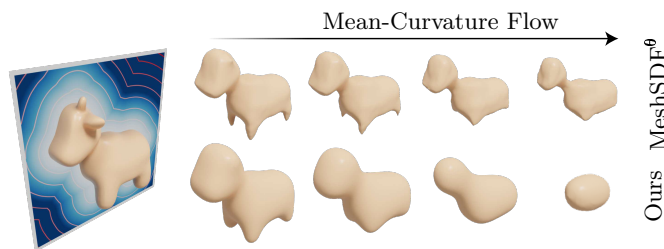

Fig. 7: We use an explicit mean-curvature flow-field to deform a parametrically defined implicit surface. When the same flow-field is used with MeshSDF, the deformation is not curvature-based. A genus-0 surface morphs into a sphere using our method while MeshSDF retains high-curvature regions.
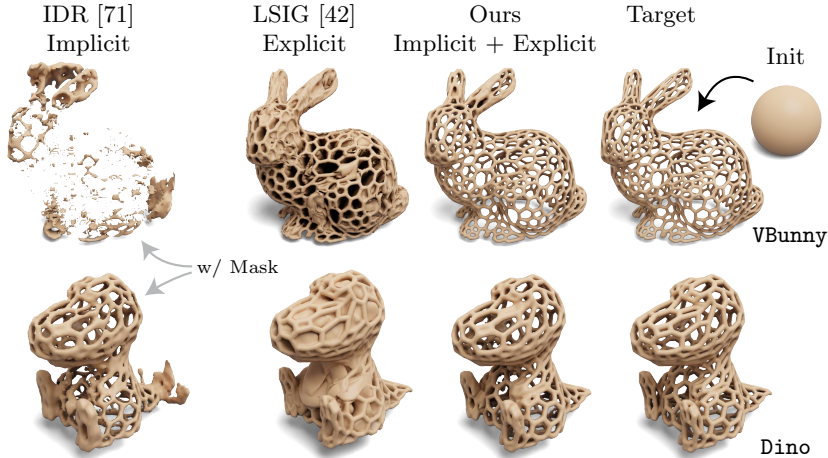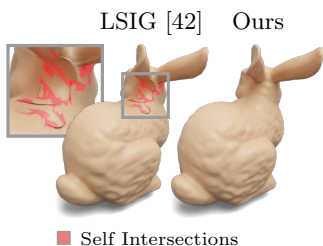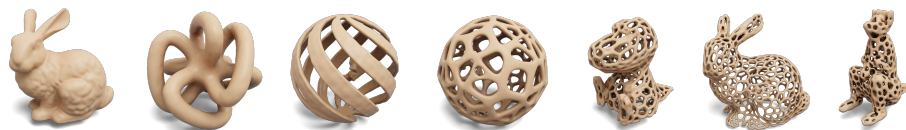
Fig. 8: **Inverse rendering of high-genus shapes.** A spherical surface is used for initialization. IDR [71], which uses differentiable rendering of implicit surfaces does not recover finer details. LSIG [42] uses a triangle-mesh and restricts the topology post initialization. Using an explicit differentiable renderer to optimize implicit geometry, our method can change topology during optimization and recover fine-details. Note that IDR requires an object mask and a neural renderer.

obtained to evolve the level-set function Φ. As a result we can take large steps in inverse rendering of geometry with unconstrained topology and guarantees on mesh quality. The resulting optimization is robust and does not require an object-mask as in the (unlike [43,71]).

We focus on geometry recovery from synthetic scenes with known reflectance. Our single-bounce forward rendering model uses a collocated camera and point-light, with a known diffuse-Phong BRDF Although we choose Nvdiffrast [28] as the differentiable rasterizer in our method, in theory it can be swapped with any other differentiable renderer. Starting from an initial estimate Φ, for each time-step t we first extract the triangle mesh $\partial\Omega_L^t$ and minimize a photometric error $\mathcal{E}$. We use the gradients of $\mathcal{E}$ to define the flow-field as $\mathbf{V}^t(\mathbf{x}_i) = -\frac{\partial\mathcal{E}}{\partial\mathbf{x}_i} - \lambda\mathbf{L}\mathbf{x}_i$, where $\mathbf{L}\mathbf{x}_i$ is used for smooth evolution. Taking a single descent step for θ is sufficient since the evolution does not need to follow a specific trajectory.

We evaluate the recovery on a diverse set of shapes, each of which is rendered from 100 random viewpoints. We use IDR [71] and LSIG [42] as baselines. We test IDR in three settings, 1) w/o Mask, 2) With known Phong shading, and 3) Using the Neural renderer in [71]. Quantitative comparisons are in Table 1 and qualitative comparisons are in Fig. 8. For a genus-0 shape (Bunny) LSIG [42] is able to recover accurate geometry, but the optimized meshes can have self

Method	Bunny	Genus6	Rind	VSphere	Dino	VBunny	Kangaroo	
IDR - w/o Mask [71]	–	–	–	–	–	–	–	
†IDR - Phong [71]	9.67	3.71	10.24	16.93	3.71	14.80	2.77	
†IDR - Neural [71]	9.84	1.35	0.21	0.16	2.07	9.11	5.43	Chamfer
LSIG [42]	0.06	2.85	3.94	4.78	2.09	4.66	1.80	×10⁻³
Ours	0.18	0.12	5.56	3.71	1.25	0.10	1.62	↓ better
†IDR - Phong [71]	21.52	18.84	15.89	18.28	20.01	17.27	21.67	
†IDR - Neural [71]	23.10	28.70	26.24	25.70	22.49	16.62	21.74	PSNR
LSIG [42]	38.51	25.67	22.81	24.06	25.11	21.77	25.52	dB
Ours	38.86	32.94	28.46	30.50	28.16	29.62	26.48	↑ better

Table 1: **Quantitative evaluation on inverse rendering of geometry.** An initial sphere is optimized to a diverse set of shapes from multi-view images. Chamfer distance is reported for geometric consistency and PSNR is reported to evaluate the visual appearance of optimized geometry. IDR [71] w/o Mask does not converge for any of the shapes. (marked –). Methods marked with † require object masks. LSIG [42] works well for a genus-0 shape (`Bunny`) but struggles with high-genus shapes. Best numbers are in orange . Shapes recovered using our method are shown on the top.

intersections as shown on the left. It struggles with high-genus shapes as the mesh connectivity remains static throughout the optimization routine. Even with correct topology at initialization, the recovery is erroneous. Comparisons with IDR [71] are in Figure 9.

6.3   User-defined Shape Editing

GT (Explicit) Ours (Implicit)

Fig. 10: User-defined editing on parametric level-sets.

We demonstrate deformation operations on parametric level-sets using constraints defined by a user. The problem setup is in line with the extensive literature [10,56,57,72] on shape editing for triangle meshes. At $t = 0$, we first extract a mesh from a neural implicit surface using MC [33]. A user can specify handle regions on this surface to either rotate, translate or freeze parts of the shape along with their target locations. This generates a sparse deformation flow-field on the surface which we *densify* by minimizing a thin-shell energy function that penalizes local stretching and bending on the surface [64]. More details are in the Appendix. Estimating the flow-field requires solving a linear system $-k_S \Delta \mathbf{V} + k_B \Delta^2 \mathbf{V} = 0$, where Δ and Δ^2 are the laplacian and bi-laplacian operators. k_S and k_B are weighting terms for stretching and bending respectively. Additional constraints which adhere to user specifications are also added to the linear system [9]. With the obtained flow-field, we update the parameters of the

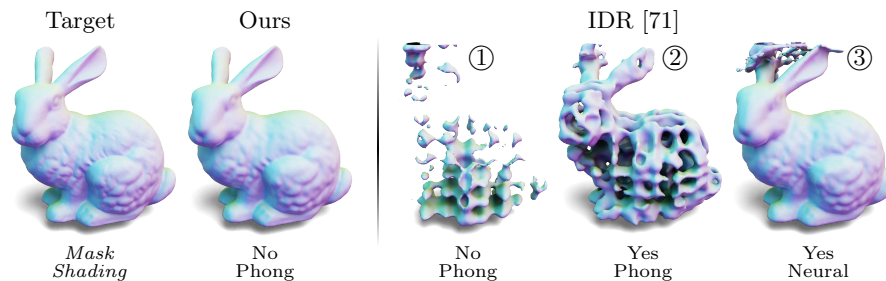Target   Ours   IDR [71]

Fig. 9: **Qualitative comparison for inverse rendering using implicit representations.** We evaluate IDR in three different settings. ① Without object-mask supervision it fails to converge to a reasonable geometry. ② With a known-reflectance model (Phong) the silhouette of the object is recovered but without any details. ③ It requires a rendering network (unknown reflectance) and an object-mask for good convergence—both of which not required for our method.

level-set function such that the surface propagation is as intended. We also use gradient regularization as in [19]. An example deformation is shown in Fig. 18.

7   Discussion

Fig. 11:   Joint recovery of geometry, complex material and lighting.

Our work formulates a level-set evolution method for parametrically defined implicit surfaces. It does not require surface extraction to be differentiable and can be used to apply mesh algorithms to neural implicit surfaces. We expect the proposed method to be particularly useful for inverse problems. We showcase one example of joint recovery of geometry, material and lighting from multi-view images in Fig. 11, where we use our surface evolution method along with components from [40]. Although the surface deformation is as dictated by the flow field, the corresponding implicit function may not retain gradient characteristics during evolution. This could become a pertinent problem for algorithms like sphere tracing [22] which require reliable distance queries, and is an interesting avenue for future research. We hope this work encourages further inquiry into recent work on geometry optimization by drawing connections to methods in computer vision and graphics developed in the pre-deep-learning era.

3dmixers users `roman_hegglin` and `PhormaSolutions` for the 3D models. We thank the anonymous reviewers for helpful comments and discussions.

8   Appendix

We organize the Appendix according to the section numbers used in the main manuscript. In Section 5.2, the proofs for Result 3 and Result 4 are outlined. In Section 6.1, implementation details are added along with additional results in Figure 12 and Figure 13. In Section 6.2, implementation details for our inverse rendering experiments are discussed and qualitative comparisons with previous works are shown in Figure 16. An inverse rendering experiment using LSIG [42] with different geometry initializations is shown in Figure 15. Section 6.3 describes the user-defined shape editing method in more detail. A comparison with NFGP [69] is in Figure 17.

5.2   Differentiable Surface Rendering

We first draw comparisons between Differentiable Volumetric Rendering[2] [43], Implicit Differentiable Renderer (IDR) [71] and Differentiable Iso-Surface Extraction in Result 3. Next, in Result 4, we show that methods in [43,71] deviate from the level-set theory for tangential flow fields.

Result 3 *Surface evolution using differentiable ray-marching of parametric implicit surfaces [38,71] is the same as using differentiable iso-surface extraction [51] when the viewing direction* $\mathbf{v}_u$ *is parallel to the normal* $\mathbf{n}$ *at the intersection point* $\mathbf{x}_u$. *The parameters* θ *for the level-set function* Φ *are updated as:*

$$\theta \leftarrow \theta - \lambda \sum_{\mathbf{x}_u} \mathbf{V} \cdot \nabla \Phi \frac{\partial \Phi}{\partial \theta}.$$

Proof. Inverse rendering methods in [43,71] find a surface-intersection point by marching a along ray that is spawned from the camera centre $\mathbf{c}$, in the direction $\mathbf{v}_u$, for each pixel u. The intersection point $\mathbf{x}_u$ is analytically defined as:

$$\mathbf{x}_u = \mathbf{c} + d_u \mathbf{v}_u, \tag{15}$$

where d_u is the depth for $\mathbf{x}_u$. The distance d_u in [43] is estimated from the camera centre. For IDR [71], the distance is computed from a point $\mathbf{y}$ close to the surface which modifies (15) to $\mathbf{x}_u = \mathbf{y}_u + d_u \mathbf{v}_u$ ($\mathbf{y}_u$ is denoted as $\mathbf{x}_0$ in [71]). In both the methods, a rendering loss function $\mathcal{L}$ (photometric error) is computed for pixels $u \in U$. To update the geometry parameters θ, the gradient $\frac{\partial \mathcal{L}}{\partial \theta}$ is computed:

$$\frac{\partial \mathcal{L}}{\partial \theta} = \sum_{u \in U} \frac{\partial \mathcal{L}}{\partial \mathbf{x}_u} \frac{\partial \mathbf{x}_u}{\partial \theta} = \sum_{u \in U} \frac{\partial \mathcal{L}}{\partial \mathbf{x}_u} \frac{\partial \mathbf{x}_u}{\partial d_u} \frac{\partial d_u}{\partial \theta} = \sum_{u \in U} \frac{\partial \mathcal{L}}{\partial \mathbf{x}_u} \cdot \mathbf{v}_u \frac{\partial d_u}{\partial \theta} \tag{16}$$

---

[2] Here, volumetric rendering is a misnomer. It's really surface rendering for geometry defined with volume/occupancy.

To compute $\frac{\partial d_u}{\partial \theta}$, we slightly deviate from the derivations in [43,71] for clarity. For points $\mathbf{x}_u$ on the implicit surface, we know $\Phi(\mathbf{x}_u) = 0$. Using implicit differentiation:

$$\frac{\partial \Phi}{\partial \theta} + \frac{\partial \Phi}{\partial \mathbf{x}_u}\frac{\partial \mathbf{x}_u}{\partial \theta} = 0$$

$$\iff \frac{\partial \Phi}{\partial \theta} + \frac{\partial \Phi}{\partial \mathbf{x}_u}\frac{\partial \mathbf{x}_u}{\partial d_u}\frac{\partial d_u}{\partial \theta} = 0$$

$$\iff \frac{\partial \Phi}{\partial \theta} + \frac{\partial \Phi}{\partial \mathbf{x}_u} \cdot \mathbf{v}_u\frac{\partial d_u}{\partial \theta} = 0 \qquad \triangleleft \text{ From (15)}$$

$$\iff \frac{\partial d_u}{\partial \theta} = -\frac{1}{\frac{\partial \Phi}{\partial \mathbf{x}_u} \cdot \mathbf{v}_u}\frac{\partial \Phi}{\partial \theta} \tag{17}$$

From (16) and (17) we have:

$$\frac{\partial \mathcal{L}}{\partial \theta} = -\sum_{u \in U}\frac{\partial \mathcal{L}}{\partial \mathbf{x}_u} \cdot \frac{\mathbf{v}_u}{\frac{\partial \Phi}{\partial \mathbf{x}_u} \cdot \mathbf{v}_u}\frac{\partial \Phi}{\partial \theta} \approx -\sum_{u \in U}\frac{\partial \mathcal{L}}{\partial \mathbf{x}_u} \cdot \frac{\nabla \Phi}{|\nabla \Phi|^2}\frac{\partial \Phi}{\partial \theta} \text{ (when } \mathbf{v}_u \to \nabla \Phi) \tag{18}$$

Taking $-\frac{\partial \mathcal{L}}{\partial \mathbf{x}_u} = \mathbf{V}$, we can update the parameters θ using (18) and gradient descent as:

$$\theta \leftarrow \theta - \lambda \sum_{\mathbf{x}_u}\mathbf{V} \cdot \nabla \Phi\frac{\partial \Phi}{\partial \theta}. \tag{19}$$

Equation (19) shows that DVR/IDR and MeshSDF$^\theta$ are closely related, while Result 1 shows that these methods do not agree with the level-set theory. $\square$

Result 4 *Differentiable ray-marching of parametric implicit surfaces [38,71] disagrees with the level-set equation for tangential components* $\mathbf{V}^\perp$ *of the flow field* $\mathbf{V}$. *The change in parameters* $\Delta\theta$ *is:*

$$\Delta\theta = \lambda \sum_{\mathbf{x}_u} \pm|\mathbf{V}^\perp|\tan(\arccos(\nabla \Phi \cdot \mathbf{v}_u))\frac{\partial \Phi}{\partial \theta}. \tag{20}$$

Proof. From (18), we know the change in parameters θ for methods in [43,71] is:

$$\Delta\theta = \lambda \sum_{\mathbf{x}_u}\mathbf{V} \cdot \frac{\mathbf{v}_u}{\nabla \Phi \cdot \mathbf{v}_u}\frac{\partial \Phi}{\partial \theta}. \tag{21}$$

When the flow-field is tangential to the surface, $\mathbf{V} = \mathbf{V}^\perp$, and $\mathbf{V}^\perp \perp \nabla \Phi$. The change in parameters for this flow-field is:

$$\Delta\theta = \lambda \sum_{\mathbf{x}_u}\frac{\mathbf{V}^\perp \cdot \mathbf{v}_u}{\nabla \Phi \cdot \mathbf{v}_u}\frac{\partial \Phi}{\partial \theta}. \tag{22}$$

Fig. 12: **Surface smoothing evolution on a half-noisy sphere.** (*Right*) Our method can evolve a noisy surface using an explicit diffusion flow-field. This allows smoothing on implicitly defined surfaces with increasing levels of smoothness. (*Left*) Yang *et al.*'s [69] method uses an optimization objective for a single level of smoothness.

When $\Phi : \mathbb{R}^2 \mapsto \mathbb{R}$ is a level-set function defined in 2D, we can modify (22) as:

$$
\begin{aligned}
\Delta\theta &= \lambda \sum_{\mathbf{x}_u} \pm |\mathbf{V}^\perp| \frac{\sin\alpha}{\cos\alpha} \frac{\partial\Phi}{\partial\theta} \qquad \text{where, } \alpha = \arccos(\nabla\phi \cdot \mathbf{v}_u) \text{ and } \Phi \text{ is an SDF} \\
&= \lambda \sum_{\mathbf{x}_u} \pm |\mathbf{V}^\perp| \tan\alpha \; \frac{\partial\Phi}{\partial\theta} \\
&= \lambda \sum_{\mathbf{x}_u} \pm |\mathbf{V}^\perp| \tan(\arccos(\nabla\Phi \cdot \mathbf{v}_u)) \; \frac{\partial\Phi}{\partial\theta}.
\end{aligned}
\tag{23}
$$

The parameters here could change depending on the angle subtended between the normal $\nabla\Phi$ and the viewing direction $\mathbf{v}_u$. This dependence on the viewing direction is a result of using differentiable ray-marching. When the function is deformed using the level-set method described in the main paper, the change in parameters $\Delta\theta$ does not depend on the viewing direction and is 0. For 3D level-set functions, the parameters could still change as the term $\mathbf{V}^\perp \cdot \mathbf{v}_u$ in (22) could be non-zero.

6.1   Curvature-based Deformation

For each shape, we optimize a SIREN [55] MLP with 5 layers, each of which has a 512-sized vector output. We use the publicly-released code[3] by Yang *et al.* [69] for SDF queries and optimization of the network. The flow-field defined in Equation (14) is used for smoothing. The learning rate is 10^{-6}, the time-delta Δt is 0.95 and an eikonal regularization term (enforcing $\nabla\Phi = 1$) [20] is used with the error function defined in Equation (5). The regularization term is weighed 10^{-3} times against the main objective. We use Adam optimizer [27] and use 200 gradient steps for each time step. The Lagrangian surface is extracted using Marching Cubes at $(120 \pm 3)^3$ resolution. Figure 12 shows the surface evolution

---

[3] https://github.com/stevenygd/NFGP

with respect to time on a half-noisy sphere (similar to [63]). In addition to the results in the main manuscript, we show qualitative comparisons with other methods in Figure 13.

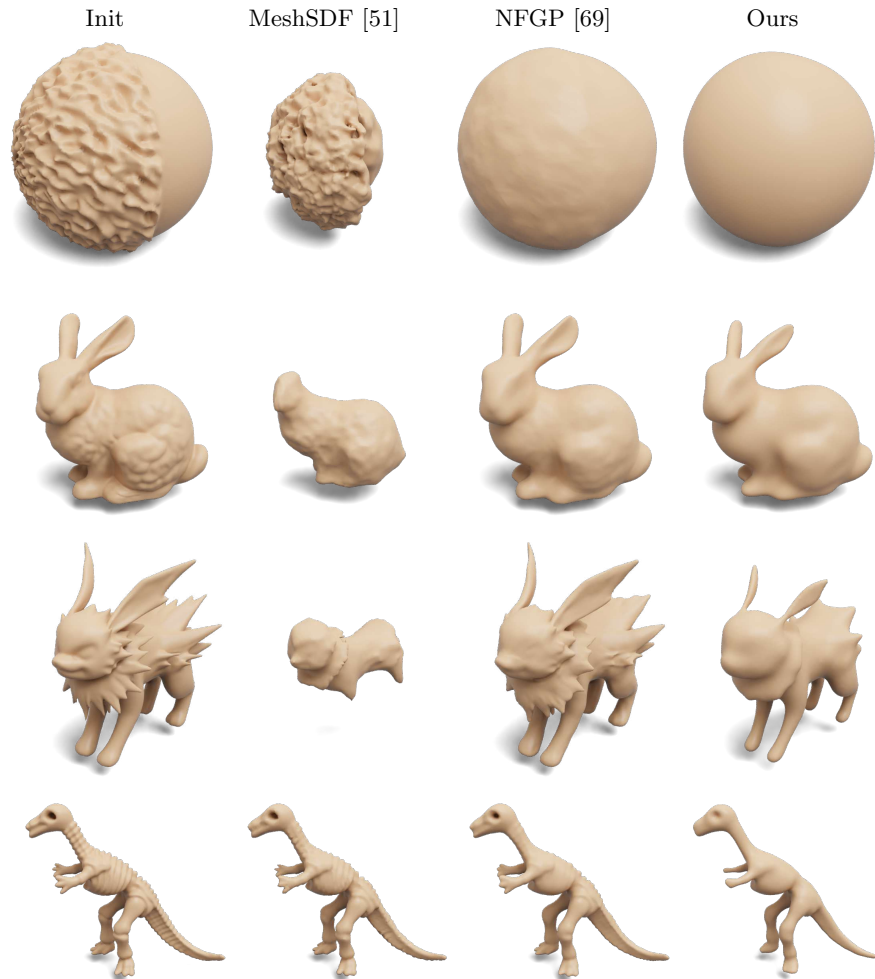| Init	MeshSDF [51]	NFGP [69]	Ours

Fig. 13: **Qualitative comparisons for surface smoothing.** We apply surface smoothing on four computer graphics models encoded as parametric level-sets. Best viewed when zoomed-in.
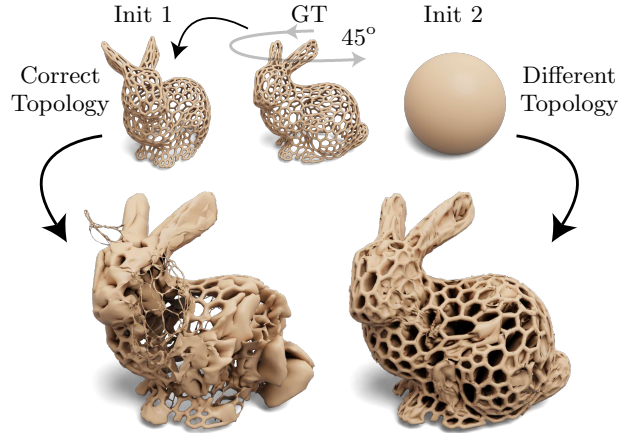
Fig. 15: **LSIG [42] converges to a poor estimate with correct topology at initialization.** Optimizing a triangle mesh for inverse rendering problems is non-trivial even when the initialization is close to the ground truth and has correct topology. For `VBunny` we rotate the target geometry and use it as initialization. The shape optimized using LSIG [42] has correct topology but with poor mesh quality and reconstruction accuracy.

6.2 Inverse Rendering

Our method uses the same spherical initialization for all the shapes. The network is composed of 4 layers, with 512 neurons in each layer. The learning-rate is 2×10^{-6}, the weight-decay factor is 0.1 and the time-delta Δt is 10^{-4}. Each object is confined in a 2^3 volume and is rendered with Nvdiffrast [28]. The weight for the smoothness regularization term linearly decreases from 10^{-3} to 0. An ablation is shown in Figure 14. We do not observe reliable improvements quantitatively with the regularizer, but do observer better

Fig. 14: Ablation on smoothness regularization term in the flow-field for inverse rendering.

convergence. The Phong shading model is used with 0.55 as the albedo value. We show an experiment with different topological initializations for LSIG [42] in Figure 15. All the qualitative comparisons for results in Table 1 (main) are in Figure 16.
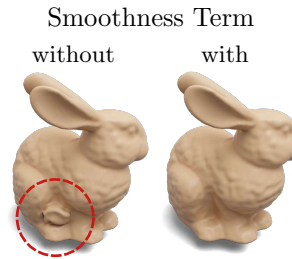
6.3 User-defined Deformation

As discussed in the main paper, we use the thin-shell energy [64] loss to densify a sparsely defined flow-field from user inputs. It induces a flow field which is

IDR	IDR	IDR	LSIG	Ours	GT
No	Yes	Yes	No	No	*Mask*
Neural	Phong	Neural	Phong	Phong	*Shading*

Fig. 16: **Qualitative comparisons for Inverse Rendering of Geometry.**

characterized using an Euler-Lagrange equation:

$$-k_s \Delta \mathbf{V} + k_b \Delta^2 \mathbf{V} = 0. \tag{24}$$

We know $\mathbf{V}$ for the regions on the surface where the user specifies the deformation and would like to estimate it for the entire surface such that there is minimum bending and stretching. Equation 24, however is a result of a linearized version of the thin-shell energy loss. In this case, the resultant deformations can be unpleasant. This is required for explicit surface deformation methods as they are expected to be conducive to real-time editing. On the contrary, our goal is to have plausible deformations which can be slightly more time consuming. For each editing operation $(\mathbf{x} \to \mathbf{x}')$, we break the deformation in T time steps as $\mathbf{x} \to \mathbf{x}^1 \to \mathbf{x}^2 \to \mathbf{x}^3 \dots \mathbf{x}^T$. For each time-step t, we solve for (24) (using a sparse linear solver) with the following user constraints:

$$\mathbf{V}(\mathbf{x}_h^{t-1}) = \mathbf{x}_h^t - \mathbf{x}_h^{t-1}, \tag{25}$$

where $\mathbf{x}_h \in \mathcal{H}$ belongs to a set of handle vertices for which the user defines deformation. Having obtained the flow-field for all the points on the surface, we evolve the surface using an Euler step as $\mathbf{x}^t = \mathbf{x}^{t-1} + \mathbf{V}(\mathbf{x}^{t-1})$. Note the absence of a delta term (Δt) in the Euler step. This is because of how we define the flow-field; we know exactly where the surface is expected to be at a given time step (From (25)). This is different from gradient-based Euler integration where we take small steps in the direction of the flow-field. Since we know *exactly* where the surface is at time t (can assume $\Phi(\mathbf{x}) = 0$ for surface points), we can tweak the objective defined in Equation 5 (main):

$$\min_{\boldsymbol{\theta}} J = \frac{1}{|\partial \Omega_L^t|} \sum_{\mathbf{x} \in \Omega_L^t} ||\Phi(\mathbf{x})||^2 + \beta \sum_{\mathbf{x} \in \Omega} (|\nabla \Phi(\mathbf{x})| - 1)^2, \tag{26}$$

where we also add Eikonal regularization. An example deformation is shown in Figure 17 including a comparison with NFGP [69]. Note that our goal with these
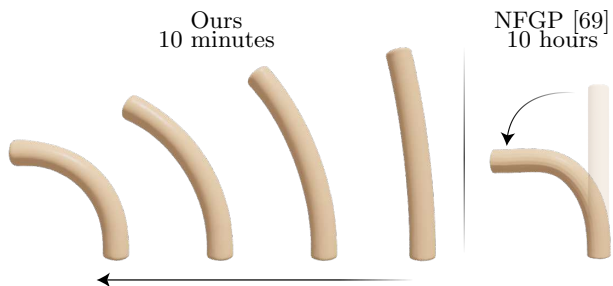

Fig. 17: **User-defined rotation on an implicitly defined cylinder.** (*Left*) User editing using our method is faster (takes 10 min) than (*Right*) NFGP which takes 10 hr for the same editing operation.
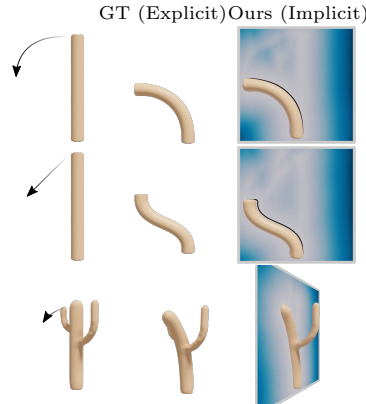
GT (Explicit) Ours (Implicit)

Fig. 18: User-defined editing on parametric level-sets.

experiments is to showcase the versatility of the level-set method and not propose a method which performs accurate and real-time deformations; we would still pose this application of user-editing as a proof of concept. Several explicit-surface based methods [8] exist which can probably generate better deformations.

Implementation Details We use pre-trained neural implicit representations provided in the publicly-released code by Yang *et al.* [69]. The number of time steps T is 20. The learning rate is 2×10^{-6} and 750 gradient steps are taken to minimize Equation 26 using Adam [27]. The regularization weighting term $\beta = 10^{-4}$.

References

1. Aliev, K.A., Sevastopolsky, A., Kolos, M., Ulyanov, D., Lempitsky, V.: Neural point-based graphics (2020)
2. Alldieck, T., Xu, H., Sminchisescu, C.: imghum: Implicit generative models of 3d human shape and articulated pose. In: Proceedings of the IEEE/CVF International Conference on Computer Vision. pp. 5461–5470 (2021)
3. Ambrosio, L., Soner, H.M.: Level set approach to mean curvature flow in arbitrary codimension. Journal of differential geometry **43**(4), 693–737 (1996)
4. Azinović, D., Li, T.M., Kaplanyan, A., Nießner, M.: Inverse path tracing for joint material and lighting estimation. In: Proc. Computer Vision and Pattern Recognition (CVPR), IEEE (2019)
5. Azinović, D., Martin-Brualla, R., Goldman, D.B., Nießner, M., Thies, J.: Neural rgb-d surface reconstruction. arXiv preprint arXiv:2104.04532 (2021)
6. Bangaru, S., Li, T.M., Durand, F.: Unbiased warped-area sampling for differentiable rendering. ACM Trans. Graph. **39**(6), 245:1–245:18 (2020)
7. Batchelor, C.K., Batchelor, G.: An introduction to fluid dynamics. Cambridge university press (2000)
8. Botsch, M., Kobbelt, L., Pauly, M., Alliez, P., Lévy, B.: Polygon mesh processing. CRC press (2010)
9. Botsch, M., Sorkine, O.: On linear variational surface deformation methods. IEEE transactions on visualization and computer graphics **14**(1), 213–230 (2007)

10. Botsch, M., Sumner, R., Pauly, M., Gross, M.: Deformation transfer for detail-preserving surface editing. In: Vision, Modeling & Visualization. pp. 357–364. Citeseer (2006)
11. Chabra, R., Lenssen, J.E., Ilg, E., Schmidt, T., Straub, J., Lovegrove, S., Newcombe, R.: Deep local shapes: Learning local sdf priors for detailed 3d reconstruction. arXiv preprint arXiv:2003.10983 (2020)
12. Chan, E.R., Monteiro, M., Kellnhofer, P., Wu, J., Wetzstein, G.: pi-gan: Periodic implicit generative adversarial networks for 3d-aware image synthesis. In: Proceedings of the IEEE/CVF conference on computer vision and pattern recognition. pp. 5799–5809 (2021)
13. Chen, Z., Zhang, H.: Learning implicit fields for generative shape modeling. In: Proceedings of the IEEE/CVF Conference on Computer Vision and Pattern Recognition (CVPR) (June 2019)
14. Chong, E.K., Zak, S.H.: An introduction to optimization. John Wiley & Sons (2004)
15. Cole, F., Genova, K., Sud, A., Vlasic, D., Zhang, Z.: Differentiable surface rendering via non-differentiable sampling. In: Proceedings of the IEEE/CVF International Conference on Computer Vision. pp. 6088–6097 (2021)
16. Davies, T., Nowrouzezahrai, D., Jacobson, A.: On the effectiveness of weight-encoded neural implicit 3d shapes. arXiv preprint arXiv:2009.09808 (2020)
17. Desbrun, M., Meyer, M., Schröder, P., Barr, A.H.: Implicit fairing of irregular meshes using diffusion and curvature flow. In: Proceedings of the 26th annual conference on Computer graphics and interactive techniques. pp. 317–324 (1999)
18. Goel, P., Cohen, L., Guesman, J., Thamizharasan, V., Tompkin, J., Ritchie, D.: Shape from tracing: Towards reconstructing 3d object geometry and svbrdf material from images via differentiable path tracing. In: 2020 International Conference on 3D Vision (3DV). pp. 1186–1195. IEEE (2020)
19. Gropp, A., Yariv, L., Haim, N., Atzmon, M., Lipman, Y.: Implicit geometric regularization for learning shapes. In: Proceedings of Machine Learning and Systems 2020 (2020)
20. Gropp, A., Yariv, L., Haim, N., Atzmon, M., Lipman, Y.: Implicit geometric regularization for learning shapes. arXiv preprint arXiv:2002.10099 (2020)
21. Gupta, K., Chandraker, M.: Neural mesh flow: 3d manifold mesh generation via diffeomorphic flows. In: Larochelle, H., Ranzato, M., Hadsell, R., Balcan, M.F., Lin, H. (eds.) Advances in Neural Information Processing Systems. vol. 33, pp. 1747–1758. Curran Associates, Inc. (2020), https://proceedings.neurips.cc/paper/2020/file/1349b36b01e0e804a6c2909a6d0ec72a-Paper.pdf
22. Hart, J.C.: Sphere tracing: A geometric method for the antialiased ray tracing of implicit surfaces. The Visual Computer **12**(10), 527–545 (1996)
23. Hasselgren, J., Hofmann, N., Munkberg, J.: Shape, light & material decomposition from images using monte carlo rendering and denoising. arXiv preprint arXiv:2206.03380 (2022)
24. Jiang, Y., Ji, D., Han, Z., Zwicker, M.: Sdfdiff: Differentiable rendering of signed distance fields for 3d shape optimization. In: Proceedings of the IEEE/CVF Conference on Computer Vision and Pattern Recognition. pp. 1251–1261 (2020)
25. Jiang, Y., Ji, D., Han, Z., Zwicker, M.: Sdfdiff: Differentiable rendering of signed distance fields for 3d shape optimization. In: The IEEE/CVF Conference on Computer Vision and Pattern Recognition (CVPR) (June 2020)
26. Kellnhofer, P., Jebe, L.C., Jones, A., Spicer, R., Pulli, K., Wetzstein, G.: Neural lumigraph rendering. In: Proceedings of the IEEE/CVF Conference on Computer Vision and Pattern Recognition. pp. 4287–4297 (2021)

27. Kingma, D.P., Ba, J.: Adam: A method for stochastic optimization. arXiv preprint arXiv:1412.6980 (2014)
28. Laine, S., Hellsten, J., Karras, T., Seol, Y., Lehtinen, J., Aila, T.: Modular primitives for high-performance differentiable rendering. ACM Transactions on Graphics **39**(6) (2020)
29. Li, T.M., Aittala, M., Durand, F., Lehtinen, J.: Differentiable monte carlo ray tracing through edge sampling. ACM Trans. Graph. (Proc. SIGGRAPH Asia) **37**(6), 222:1–222:11 (2018)
30. Liu, H.T.D., Williams, F., Jacobson, A., Fidler, S., Litany, O.: Learning smooth neural functions via lipschitz regularization. arXiv preprint arXiv:2202.08345 (2022)
31. Liu, S., Zhang, Y., Peng, S., Shi, B., Pollefeys, M., Cui, Z.: Dist: Rendering deep implicit signed distance function with differentiable sphere tracing. In: IEEE/CVF Conference on Computer Vision and Pattern Recognition (CVPR) (June 2020)
32. Liu, S., Li, T., Chen, W., Li, H.: Soft rasterizer: A differentiable renderer for image-based 3d reasoning. The IEEE International Conference on Computer Vision (ICCV) (Oct 2019)
33. Lorensen, W.E., Cline, H.E.: Marching cubes: A high resolution 3d surface construction algorithm. ACM siggraph computer graphics **21**(4), 163–169 (1987)
34. Luan, F., Zhao, S., Bala, K., Dong, Z.: Unified shape and svbrdf recovery using differentiable monte carlo rendering. ArXiv (2021)
35. Markstein, G.H.: Nonsteady flame propagation: AGARDograph. Elsevier (2014)
36. Martel, J.N.P., Lindell, D.B., Lin, C.Z., Chan, E.R., Monteiro, M., Wetzstein, G.: Acorn: Adaptive coordinate networks for neural scene representation. ACM Trans. Graph. (SIGGRAPH) **40**(4) (2021)
37. Mehta, I., Gharbi, M., Barnes, C., Shechtman, E., Ramamoorthi, R., Chandraker, M.: Modulated periodic activations for generalizable local functional representations. In: Proceedings of the IEEE/CVF International Conference on Computer Vision (ICCV). pp. 14214–14223 (October 2021)
38. Mescheder, L., Oechsle, M., Niemeyer, M., Nowozin, S., Geiger, A.: Occupancy networks: Learning 3d reconstruction in function space. In: Proceedings IEEE Conf. on Computer Vision and Pattern Recognition (CVPR) (2019)
39. Mu, J., Qiu, W., Kortylewski, A., Yuille, A., Vasconcelos, N., Wang, X.: A-sdf: Learning disentangled signed distance functions for articulated shape representation. In: Proceedings of the IEEE/CVF International Conference on Computer Vision. pp. 13001–13011 (2021)
40. Munkberg, J., Hasselgren, J., Shen, T., Gao, J., Chen, W., Evans, A., Mueller, T., Fidler, S.: Extracting Triangular 3D Models, Materials, and Lighting From Images. arXiv:2111.12503 (2021)
41. Museth, K., Breen, D.E., Whitaker, R.T., Barr, A.H.: Level set surface editing operators. In: Proceedings of the 29th annual conference on Computer graphics and interactive techniques. pp. 330–338 (2002)
42. Nicolet, B., Jacobson, A., Jakob, W.: Large steps in inverse rendering of geometry. ACM Transactions on Graphics (Proceedings of SIGGRAPH Asia) **40**(6) (Dec 2021). https://doi.org/10.1145/3478513.3480501, `https://rgl.epfl.ch/publications/Nicolet2021Large`
43. Niemeyer, M., Mescheder, L., Oechsle, M., Geiger, A.: Differentiable volumetric rendering: Learning implicit 3d representations without 3d supervision. In: IEEE/CVF Conference on Computer Vision and Pattern Recognition (CVPR) (June 2020)
44. Nimier-David, M., Vicini, D., Zeltner, T., Jakob, W.: Mitsuba 2: A retargetable forward and inverse renderer. Transactions on Graphics (Proceedings of SIGGRAPH Asia) **38**(6) (Dec 2019). https://doi.org/10.1145/3355089.3356498

45. Oechsle, M., Peng, S., Geiger, A.: Unisurf: Unifying neural implicit surfaces and radiance fields for multi-view reconstruction. In: Proceedings of the IEEE/CVF International Conference on Computer Vision. pp. 5589–5599 (2021)
46. Osher, S., Fedkiw, R.P.: Level set methods: an overview and some recent results. Journal of Computational physics **169**(2), 463–502 (2001)
47. Osher, S., Sethian, J.A.: Fronts propagating with curvature-dependent speed: Algorithms based on hamilton-jacobi formulations. Journal of computational physics (1988)
48. Park, J.J., Florence, P., Straub, J., Newcombe, R., Lovegrove, S.: Deepsdf: Learning continuous signed distance functions for shape representation. In: Proceedings of the IEEE/CVF Conference on Computer Vision and Pattern Recognition (CVPR) (June 2019)
49. Quilez, I.: `https:iquilezles.org/www/articles/distfunctions/distfunctions.htm`
50. Ravi, N., Reizenstein, J., Novotny, D., Gordon, T., Lo, W.Y., Johnson, J., Gkioxari, G.: Accelerating 3d deep learning with pytorch3d. arXiv:2007.08501 (2020)
51. Remelli, E., Lukoianov, A., Richter, S., Guillard, B., Bagautdinov, T., Baque, P., Fua, P.: Meshsdf: Differentiable iso-surface extraction. In: Larochelle, H., Ranzato, M., Hadsell, R., Balcan, M.F., Lin, H. (eds.) Advances in Neural Information Processing Systems. vol. 33, pp. 22468–22478. Curran Associates, Inc. (2020), `https://proceedings.neurips.cc/paper/2020/file/fe40fb944ee700392ed51bfe84dd4e3d-Paper.pdf`
52. Rückert, D., Franke, L., Stamminger, M.: Adop: Approximate differentiable one-pixel point rendering. arXiv preprint arXiv:2110.06635 (2021)
53. Shen, T., Gao, J., Yin, K., Liu, M.Y., Fidler, S.: Deep marching tetrahedra: a hybrid representation for high-resolution 3d shape synthesis. In: Advances in Neural Information Processing Systems (NeurIPS) (2021)
54. Sitzmann, V., Chan, E.R., Tucker, R., Snavely, N., Wetzstein, G.: Metasdf: Meta-learning signed distance functions. In: Proc. NeurIPS (2020)
55. Sitzmann, V., Martel, J.N., Bergman, A.W., Lindell, D.B., Wetzstein, G.: Implicit neural representations with periodic activation functions. In: arXiv (2020)
56. Sorkine, O., Alexa, M.: As-rigid-as-possible surface modeling. In: Symposium on Geometry processing. vol. 4, pp. 109–116 (2007)
57. Sorkine, O., Cohen-Or, D., Lipman, Y., Alexa, M., Rössl, C., Seidel, H.P.: Laplacian surface editing. In: Proceedings of the 2004 Eurographics/ACM SIGGRAPH symposium on Geometry processing. pp. 175–184 (2004)
58. Stanley, K.O.: Compositional pattern producing networks: A novel abstraction of development. Genetic programming and evolvable machines **8**(2), 131–162 (2007)
59. Sucar, E., Liu, S., Ortiz, J., Davison, A.J.: imap: Implicit mapping and positioning in real-time. In: Proceedings of the IEEE/CVF International Conference on Computer Vision. pp. 6229–6238 (2021)
60. Süli, E., Mayers, D.: An Introduction to Numerical Analysis. An Introduction to Numerical Analysis, Cambridge University Press (2003), `https://books.google.com/books?id=hj9weaqJTbQC`
61. Takikawa, T., Litalien, J., Yin, K., Kreis, K., Loop, C., Nowrouzezahrai, D., Jacobson, A., McGuire, M., Fidler, S.: Neural geometric level of detail: Real-time rendering with implicit 3D shapes (2021)
62. Tancik, M., Srinivasan, P.P., Mildenhall, B., Fridovich-Keil, S., Raghavan, N., Singhal, U., Ramamoorthi, R., Barron, J.T., Ng, R.: Fourier features let networks learn high frequency functions in low dimensional domains. arXiv preprint arXiv:2006.10739 (2020)

63. Taubin, G.: A signal processing approach to fair surface design. In: Proceedings of the 22nd annual conference on Computer graphics and interactive techniques. pp. 351–358 (1995)
64. Terzopoulos, D., Platt, J., Barr, A., Fleischer, K.: Elastically deformable models. In: Proceedings of the 14th annual conference on Computer graphics and interactive techniques. pp. 205–214 (1987)
65. Tewari, A., Thies, J., Mildenhall, B., Srinivasan, P., Tretschk, E., Wang, Y., Lassner, C., Sitzmann, V., Martin-Brualla, R., Lombardi, S., et al.: Advances in neural rendering. arXiv preprint arXiv:2111.05849 (2021)
66. Whitaker, R.T.: A level-set approach to 3d reconstruction from range data. International journal of computer vision $\mathbf{29}$(3), 203–231 (1998)
67. Xie, Y., Takikawa, T., Saito, S., Litany, O., Yan, S., Khan, N., Tombari, F., Tompkin, J., Sitzmann, V., Sridhar, S.: Neural fields in visual computing and beyond. arXiv preprint arXiv:2111.11426 (2021)
68. Xu, Y., Peng, S., Yang, C., Shen, Y., Zhou, B.: 3d-aware image synthesis via learning structural and textural representations (2021)
69. Yang, G., Belongie, S., Hariharan, B., Koltun, V.: Geometry processing with neural fields. In: Thirty-Fifth Conference on Neural Information Processing Systems (2021)
70. Yariv, L., Gu, J., Kasten, Y., Lipman, Y.: Volume rendering of neural implicit surfaces. Advances in Neural Information Processing Systems $\mathbf{34}$ (2021)
71. Yariv, L., Kasten, Y., Moran, D., Galun, M., Atzmon, M., Ronen, B., Lipman, Y.: Multiview neural surface reconstruction by disentangling geometry and appearance. Advances in Neural Information Processing Systems $\mathbf{33}$ (2020)
72. Zayer, R., Rössl, C., Karni, Z., Seidel, H.P.: Harmonic guidance for surface deformation. In: Computer Graphics Forum. vol. 24, pp. 601–609. Citeseer (2005)
73. Zhang, C., Miller, B., Yan, K., Gkioulekas, I., Zhao, S.: Path-space differentiable rendering. ACM Trans. Graph. $\mathbf{39}$(4), 143:1–143:19 (2020)
74. Zhu, Z., Peng, S., Larsson, V., Xu, W., Bao, H., Cui, Z., Oswald, M.R., Pollefeys, M.: Nice-slam: Neural implicit scalable encoding for slam. arXiv preprint arXiv:2112.12130 (2021)